

# Enhanced cycling performance of a high-energy and low-cost lithium–sulfur battery with a sulfur/hardwood charcoal composite cathode material

Kazem Jeddi · Kaveh Sarikhani · Mahmoudreza Ghaznavi ·  
Sohrab Zendehtoodi · P. Chen

Received: 23 September 2014 / Revised: 13 December 2014 / Accepted: 20 December 2014 / Published online: 10 January 2015  
© Springer-Verlag Berlin Heidelberg 2015

**Abstract** Lithium–sulfur battery is an attractive candidate for advanced energy storage devices due to its high specific energy of  $2600 \text{ Wh kg}^{-1}$  arising from the high theoretical specific capacity ( $1675 \text{ mAh g}^{-1}$ ) of the sulfur cathode. However, short cycle life and low cycling efficiency are still the main obstacles preventing the practical development of this promising battery system. In this work, we show that a low-cost Li/S cell employing an activated hardwood charcoal–sulfur (S–AHC) nanocomposite cathode can be operated for more than 300 cycles while still maintaining high specific capacity ( $600 \text{ mAh g}^{-1}$ ) and coulombic efficiency of 97 %, achieved by a new formulation of liquid electrolyte containing a fluorinated solvent. Such an improved capacity retention and cycle life, as compared to its conventional counterparts, prove that active mass lost via polysulfide dissolution can be effectively inhibited by utilization of this liquid electrolyte solution. Considering these results, we believe that the Li/S battery consisted of this composite cathode and the liquid electrolyte may be proposed as a promising candidate for low-cost energy storage applications.

**Keywords** Lithium–sulfur battery · Liquid electrolyte · Cycle life · Hardwood charcoal

## Introduction

In the recent years, there has been a steadily increasing interest in developing lithium–ion rechargeable batteries with high specific energy, to extend their application to the fields of emerging technologies, such as electric vehicles (EV) and long-lasting portable electronic devices [1, 2]. Limited by the relatively low capacity of cathode materials, present lithium–ion batteries have practical energy density of below  $300 \text{ Wh kg}^{-1}$ , which is insufficient for most of the aforementioned applications [3]. In this regard, alternative electrode materials with much higher charge capacities are of great interest. Sulfur possesses a theoretical specific capacity of  $1672 \text{ mAh g}^{-1}$  and specific energy of  $2600 \text{ Wh kg}^{-1}$ , when the complete reaction of lithium with sulfur is assumed [4, 5]. In addition, the abundance and low price of sulfur offer the opportunity of producing cheap, safe, and high-energy density cathodes. In contrast to conventional lithium–ion batteries, lithium–sulfur (Li/S) batteries operate on “integration chemistry,” which enables the battery cell to tolerate excess charges or discharges, minimizing overcharge dangers often happening in other lithium–ion batteries [6, 7].

Despite these advantages, practical development of Li/S batteries is still prevented by low cyclability and low utilization of active materials, due to the poor electronic conductivity of sulfur, dissolution of lithium polysulfides, which are intermediate products generated during discharge, and their high reactivity with the anode, together with significant volume change upon lithiation [8, 9]. To overcome these drawbacks, a large number of studies have focused on increasing the electronic conductivity of sulfur and suppressing the polysulfide dissolution into the liquid electrolyte [10–14]. Encapsulating sulfur molecules with conducting materials, such as porous carbon or conductive polymers, enables them to become electrically wired and therefore electrochemically active. Conductive polymers such as polyacrylonitrile (PAN) [15, 16] and polypyrrole (PPY) [17,

**Electronic supplementary material** The online version of this article (doi:10.1007/s10008-014-2721-7) contains supplementary material, which is available to authorized users.

K. Jeddi · K. Sarikhani · M. Ghaznavi · S. Zendehtoodi ·  
P. Chen (✉)

Waterloo Institute for Nanotechnology and Department of Chemical  
Engineering, University of Waterloo, Waterloo,  
ON N2L 3G1, Canada  
e-mail: p4chen@uwaterloo.ca

[18] are usually used to prepare sulfur–polymer composites. Although sulfur/polymer composites generally improve the cycling performance of Li/S cells, it should be pointed out that in all of these composites, a large amount of the conductive polymer should be mixed into the cathode, resulting in low sulfur content of the electrode. As a result, the implication of this strategy seems to be more academic than practical [19]. On the other hand, a sulfur/carbon (S/C) composite potentially offers higher loading of sulfur. Various carbon materials, such as mesoporous carbon, carbon nanofibers, carbon nanotubes, and carbon spheres have been used in preparing S/C composites. However, poor cyclability and low cycling efficiency still remained [10–14, 20, 21]. A few recent studies have reported application of activated carbon with high porosity and surface area in preparing sulfur composite cathodes [22, 23]. Activated carbon is a cheap and abundant material, which can be easily obtained from the carbonization of different materials such as wood, coal, and lignite [23].

Very recently, researchers have considered addition of a fluorinated solvent into the electrolyte solution to suppress the dissolution of lithium polysulfide and prevent the shuttle effect [24, 25]. The resulting Li/S battery showed improved cyclability and coulombic efficiency over a very limited number of cycles, which were too small for any possible practical applications. In order to be relevant, Li/S batteries have to demonstrate cycle life as long as that of lithium–ion batteries. In this study, we aim to utilize the same strategy in order to stabilize sulfur-activated hardwood charcoal composite, a low-cost and environmentally benign cathode material, with a prolonged cycle life. Activated hardwood charcoal (AHC) is an odorless, tasteless, and nontoxic powder derived from chips and sawdust with a high surface area ( $1400\text{--}1800\text{ m}^2\text{ g}^{-1}$ ), which can be used in poultices for external treatment of localized inflammation, infection, and pain. Moreover, AHC is completely safe, even for oral use, allowing it to be added to animal food for treating poisoning, infection, and foul odors. Owing to its high porosity, specific surface area, and good electrical conductivity, AHC may provide a unique scaffold to embed sulfur to improve the electronic conductivity of sulfur active material. Utilization of AHC, an inexpensive and abundant source of carbon, can significantly lower the final cost of the battery preparation. The obtained results prove that utilization of this liquid electrolyte dramatically improves the discharge capacity retention and coulombic efficiency of this high-energy and low-cost Li/S energy storage system.

## Experimental

### Material preparation

An activated hardwood charcoal (AHC) powder was purchased from *buyactivatedcharcoal.com* and was pre-heated

at  $800\text{ }^\circ\text{C}$  for 3 h. The Brunauer–Emmett–Teller (BET) analysis confirmed the pore volume and specific surface area of the AHC to be  $1.12\text{ cm}^3\text{ g}^{-1}$  and  $1747.3\text{ m}^2\text{ g}^{-1}$ , respectively. Sulfur (100-mesh particle size powder, Sigma-Aldrich) and AHC powder in a weight ratio of 10:4 was used to prepare the S–AHC composite by employing a solution processing method [23]. First, sulfur powder was dissolved in dimethyl sulfoxide (DMSO) at  $120\text{ }^\circ\text{C}$  by vigorously stirring for 2 h. Then, the AHC powder was added to the solution and dispersed by stirring for 4 h. This was followed by gradually cooling the mixture to room temperature while being stirred overnight. Within the cooling process, the dissolved sulfur molecules were recrystallized in the highly porous structure of the AHC, resulting in a sulfur–carbon composite. Finally, the composite powder was washed with ethanol and ultrapure water several times and then dried in a vacuum at  $100\text{ }^\circ\text{C}$  to evaporate ethanol, water, and residual DMSO.

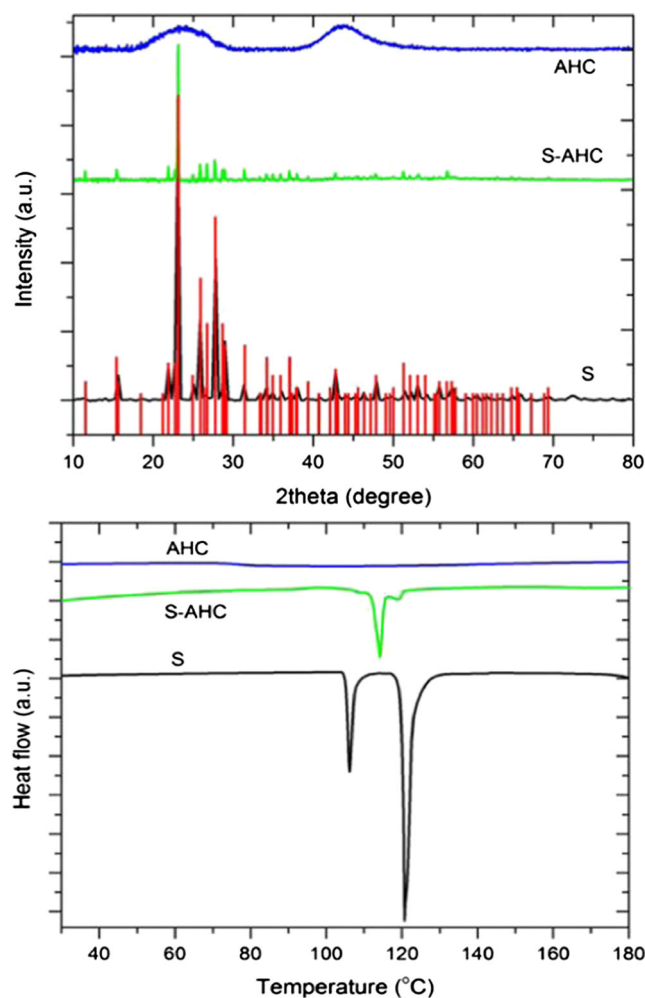
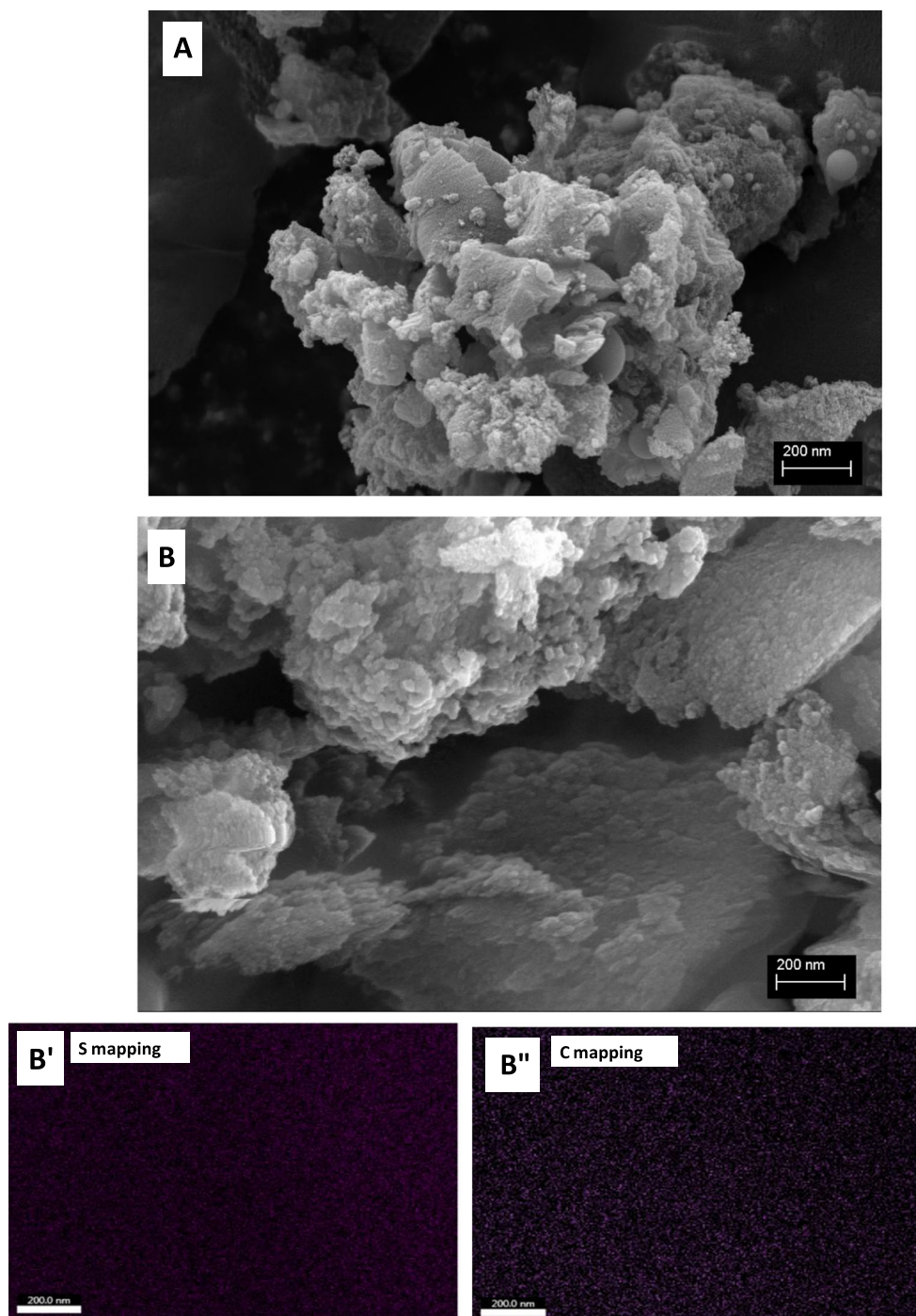


**Fig. 1** XRD patterns (*top*) and DSC curves (*bottom*) for elemental sulfur, activated hardwood charcoal, and the S–AHC composite

**Fig. 2** SEM images for **a** AHC powder and **b** S–AHC nanocomposite powder. (*B'*, *B''*) show the S mapping and C mapping of the S–AHC nanocomposite



#### Characterization of the materials

X-ray diffraction (XRD) patterns were obtained on a D8 Discover Bruker instrument equipped with Cu-K $\alpha$  radiation. SEM images were taken using a field emission scanning electron microscopy (FE-SEM) (Leo-1530, Zeiss). The samples were gold-sprayed prior to SEM measurements. The interior morphology of the samples was further studied using transmission electron microscopy (TEM, CM10, Philips). The

state of sulfur in the S–AHC composite was studied by UV–vis absorption spectroscopy (Ultrospec 4300 Pro) with 1 nm resolution on powders dispersed in ethanol through ultrasonication for 3 h. Thermogravimetric analysis (TGA) was carried out using a DSC-TGA (Q-600, TA instruments) at temperature ramp mode with a heating rate of 10 °C min<sup>-1</sup> at N<sub>2</sub> gas atmosphere. Nitrogen adsorption–desorption isotherms were measured at 77 K with a surface area analyzer (ASAP 2020). Prior to the measurements, the samples were

degassed at 300 °C for at least 24 h. The Brunauer–Emmett–Teller (BET) method was used to calculate the specific surface area. The Barrett–Joyner–Halenda (BJH) model was also used to calculate the pore size and volume.

### Electrochemical characterization

The S–AHC cathode electrode was prepared by mixing of 70 wt% S–AHC composite, 20 wt% acetylene black (AB, MTI, 99.5 % purity) as conductive agent, and 10 wt% polyvinylidene fluoride (PVDF, Kynar, HSV900) as a binder with NMP (Sigma-Aldrich,  $\geq 99.5$  % purity) as a dispersant. The resultant slurry was spread uniformly onto an Al foil using the doctor blade technique (the gap size of the blade was 200  $\mu\text{m}$ ) and then vacuum dried at 70 °C for 12 h. The electrochemical properties were investigated using coin-type cells (CR2032). Each cell was composed of a lithium metal anode, a sulfur-based composite cathode, and an electrolyte (a polypropylene separator (Celgard, USA) with 1 M LiTFSI dissolved in a 1:1 (v/v) mixture of 1,3-dioxolane (DOL) and 1, 1,2,2-tetrafluoroethyl-2,2,3,3-tetrafluoropropyl ether (TTE)). A 1 M LiTFSI dissolved in a 1:1 (v/v) mixture of DOL and 1, 2-dimethoxyethane (DME) was used a reference electrolyte solution. A galvanostatic charge/discharge test was carried out within a voltage range of 1.5–2.8 V, at a discharge rate of either 0.1 C or 0.3 C (1 C = 1672 mAh  $\text{g}^{-1}$ ). Cyclic voltammetry (CV) measurements were done at a scanning rate of 0.05 mV  $\text{s}^{-1}$ .

### Results and discussion

The morphology of S–AHC composite was experimentally studied using XRD, DSC, TGA, SEM, TEM, and BET. Figure 1 (top) shows the XRD spectra of pristine sulfur, AHC, and S–AHC composite. The pattern observed for pristine sulfur matches very well with the standard of orthorhombic phase sulfur while the pattern of the S–AHC composite shows a broad diffraction peak at around 25° and low intensity diffraction peaks of crystal sulfur, which could be an indication recrystallization of sulfur into the internal pores or surface of AHC particles. Figure 1(bottom) shows the heat flow versus temperature curves for sulfur, AHC powder, and S–AHC composite. The pristine sulfur shows two sharp endothermic peaks at 110 and 120 °C arising from the phase transition and melting of the elemental sulfur. However, the S–AHC composite shows only one endothermic peak with relatively lower intensity at 115 °C attributed to the melting of nano-sized elemental sulfur [23]. SEM and TEM images for AHC and S–AHC composite powders at two magnifications are shown in Figs. 2 and S1, respectively. These images show the high surface area and pore volume of the AHC powder.

The as-prepared S–AHC composite aggregates have a particle size of a few hundred nanometers. Moreover, BET results confirmed that the specific surface area of AHC powder reduces from 1747.3 to 541.17  $\text{m}^2 \text{g}^{-1}$  and particle size increases from 3.43 to 11.08 nm when the S–AHC composite is formed. Results of energy-dispersive X-ray spectroscopy (EDX) mapping for both of sulfur (S) and carbon (C) are also shown in Fig. 2. These results point out that sulfur is either embedded in the micropores of AHC particles or deposited on its surface and distributed uniformly within the composite. During the composite preparation process, sulfur was dissolved and uniformly mixed with AHC matrix. Later in the cooling process, sulfur re-crystallized and was homogeneously distributed in the matrix. As a result, the crystal size of sulfur was considerably reduced after this dissolution and re-crystallization process, allowing the formation of S–AHC composite containing crystalline sulfur with smaller particle size.

Thermogravimetric analysis (TGA) was used to determine the sulfur content in the S–AHC composite, and the results are shown in Fig. 3. Sulfur is stable up to 220 °C, and a rapid weight loss happens at 220–310 °C pointing out a very rapid decomposition process and fast migration of degradation products from the remaining mass. However, the weight loss of the S–AHC composite occurs in the range of 220–380 °C with a mass remaining of 35 wt%. Above 380 °C, there was no weight change. This shows that S–AHC composite contains 65 wt% sulfur, which is higher than the previously reported work [23]. This is due to the high surface area and porosity of activated hardwood charcoal (AHC) that offers higher loading of sulfur compared to conventional carbon sources.

UV–vis spectroscopy was used to study the state of sulfur within the composite. Figure S2 shows the obtained spectra for pristine sulfur, AHC powder, and S–AHC composite.

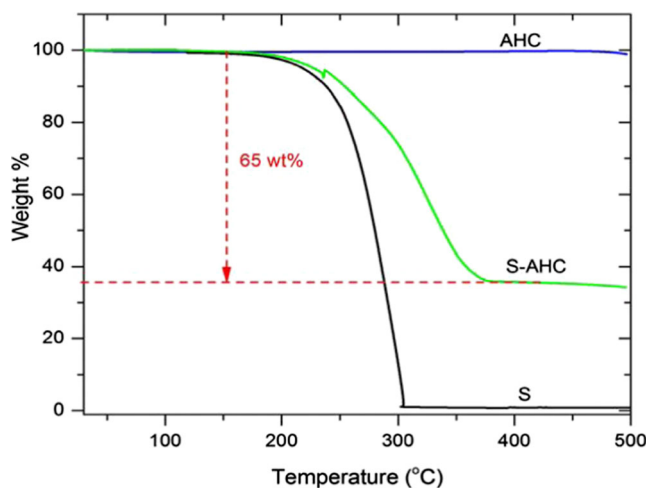


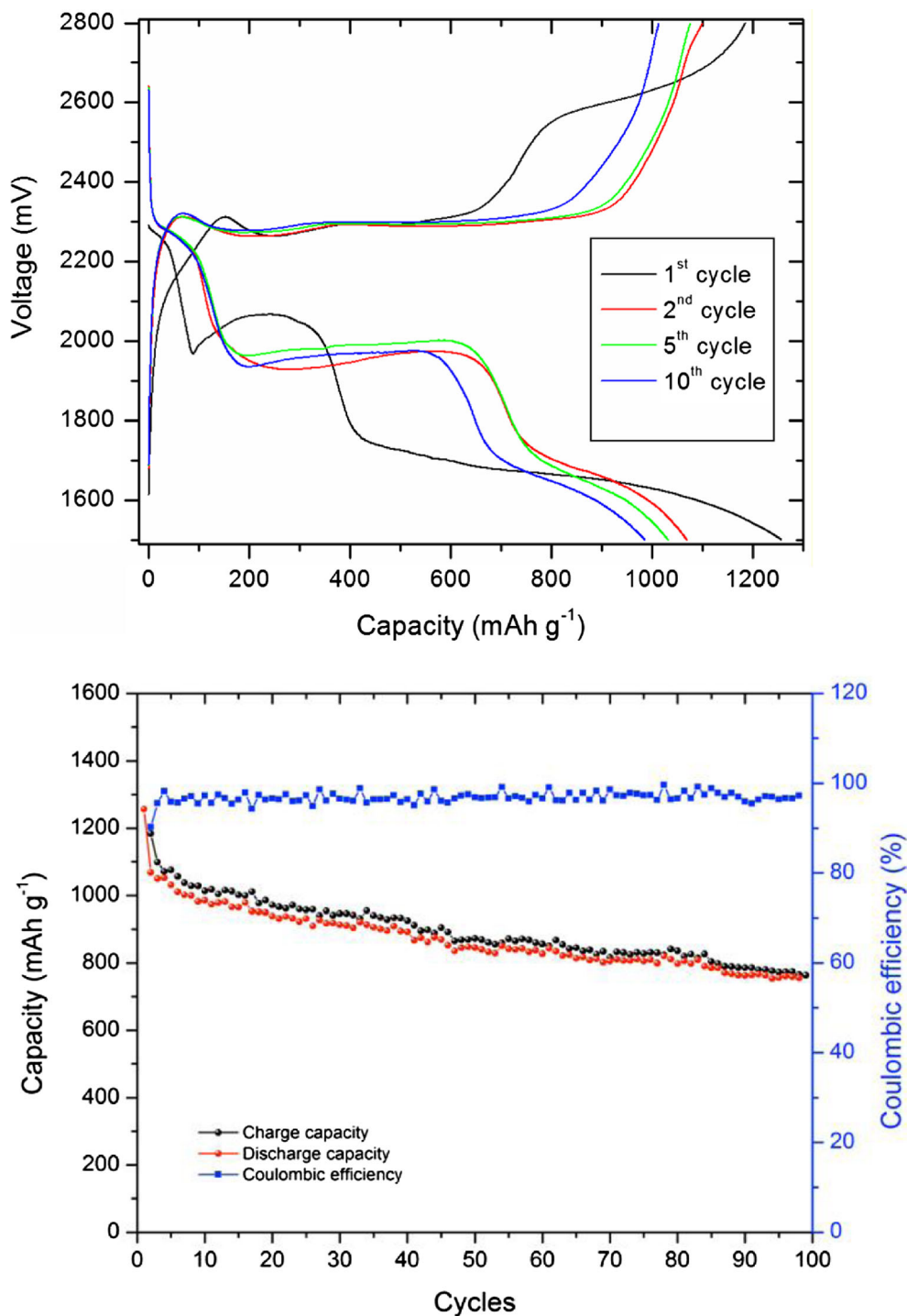
**Fig. 3** Thermogravimetric analysis graphs for sulfur, activated hardwood charcoal, and S–AHC composite



AHC shows no absorption peak while pristine sulfur shows a broad absorption peak between 200 and 350 nm, which is attributed to the elemental sulfur. As can be seen, the S–AHC composite has similar absorption spectra with sulfur, indicating that no chemical reaction takes place between sulfur and AHC under this synthesis condition, and sulfur inside the micropores or on the surface of AHC powder remains in its elemental state.

Figure 4 presents charge–discharge profiles and cycling for this Li/S battery cell. An initial discharge capacity of  $1260 \text{ mAh g}^{-1}$  (based on the sulfur mass in the composite cathode) is obtained. A stable discharge capacity of  $800 \text{ mAh g}^{-1}$  and a coulombic efficiency of 97 % are obtained after 100 cycles at 0.1 C, indicating a very good cyclability of this battery cell. To compare the improvement in the electrochemical performance, a Li/S cell with the conventional

**Fig. 4** Charge–discharge profiles and cycling performance of the Li/S cell with the fluorinated electrolyte at a 0.1 C rate and 1.5–2.8 V voltage range



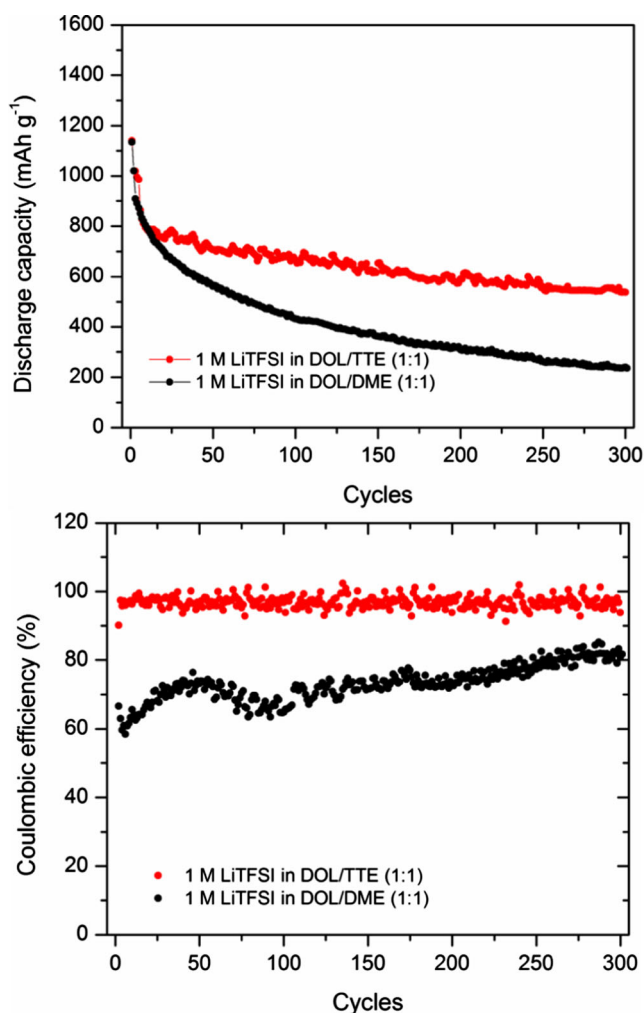


**Fig. 5** Comparison of the cyclic performance (*top*) and coulombic efficiency (*bottom*) of two Li/S cells with different electrolytes at 0.3 C rate and 1.5–2.8 V voltage range

electrolyte solution (1 M LiTFSI in DOL/DME) was also tested under the same testing condition to be used as a reference. Capacity retention and cycling efficiency versus cycles

for these two Li/S cells are shown in Fig. 5. The Li–S cell using the reference electrolyte solution shows low coulombic efficiency and its capacity decreases rapidly over cycling. A discharge capacity of 230 mAh g<sup>-1</sup> and coulombic efficiency of 80 % are obtained after 300 cycles. Such a poor cyclability and low efficiency are attributed to the dissolution of lithium polysulfide intermediates into the electrolyte resulting in a severe active mass loss and shuttle reactions of these soluble species during the charge and discharge processes, hence reducing the discharge capacity and increasing the charge capacity [26, 27]. In contrast, the Li/S cell with the new electrolyte solution shows significantly improved cyclability and higher coulombic efficiency, delivering capacity of about 600 mAh g<sup>-1</sup> and maintaining a coulombic efficiency of 97 % after 300 cycles.

Cyclic voltammetry (CV) measurements were used to identify the electrochemical properties of both cells, and the results are presented in Fig. 6. For the cell with the reference electrolyte, typical characteristics of multistep electrochemical reactions between sulfur and lithium ions are observed by two oxidation peaks at 2.3 and 2.05 V, together with corresponding reduction peak at 2.35 V. On the other hand, the cell with the fluorinated electrolyte exhibited a relatively different trend, as the two oxidation peaks are located at 2.25 and 1.8 V. Moreover, the reduction peak is located at above 2.4 V, and a small shoulder is observed at a voltage slightly below 2.4 V. These shifts in the oxidation peaks toward lower potential and in the reduction peak toward higher potential in the cell with the fluorinated electrolyte indicates lower ionic conductivity arising from lower concentration of dissolved polysulfides in this electrolyte. Another noticeable difference in the CV graphs is the lower altitude of the reduction and oxidation peaks in the cell with the fluorinated electrolyte compared to the reference electrolyte, which is an indication of slow reaction kinetics in this cell, most probably because of lower concentrations of polysulfides.

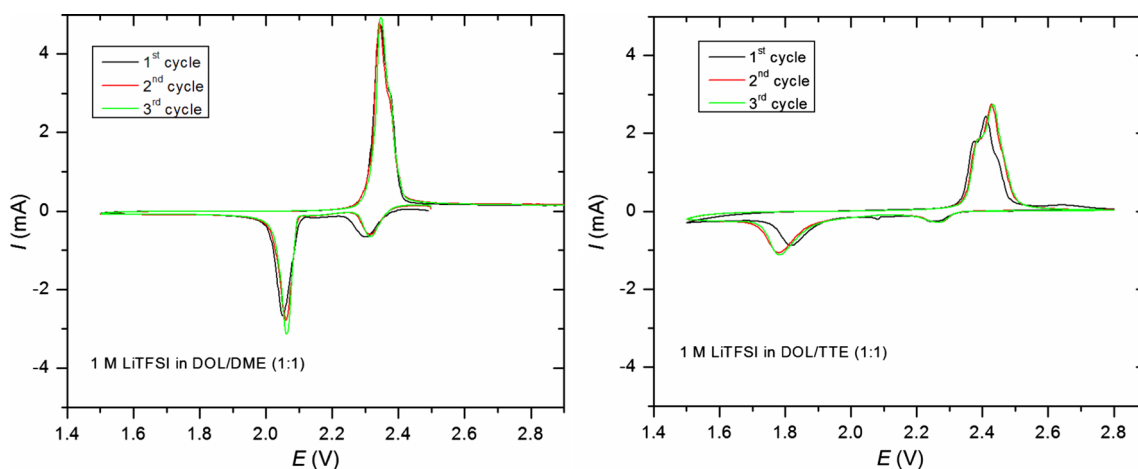


**Fig. 6** Cyclic voltammetry of both Li/S cells at a scanning rate of 0.05 mV s<sup>-1</sup>

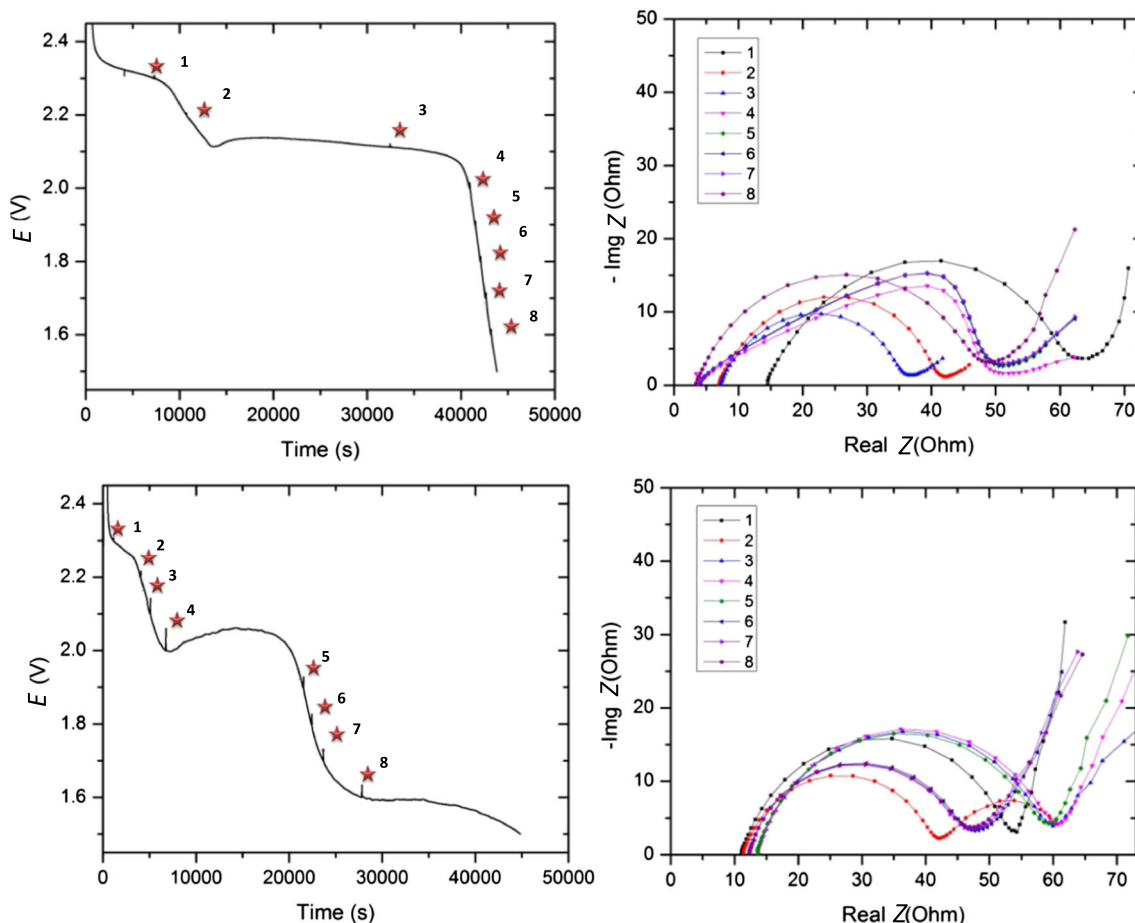


**Fig. 7** GITT and AC impedance spectroscopy results obtained at the first discharge process for the Li/S cell with two different liquid electrolytes. 1 M LiTFSI in DOL/DME (1:1) (*top*) and 1 M LiTFSI in DOL/TTE (*bottom*)

Galvanostatic intermittent titration technique (GITT) experiments were also conducted with a BioLogic electrochemical instrument to further study the electrochemical reactions as a function of depth of discharge (Fig. 7). The cells were discharged with a slow current rate of 0.05 C (83.6 mA g<sup>-1</sup>) in the voltage range of 2.5–1.5 V. Then, AC impedance spectroscopy was performed at each point with different depth of discharge (DOD). The impedance spectra were collected at room temperature with amplitude of 10 mV in the frequency range of 1 MHz to 100 mHz. The equivalent circuit (EC) fitting applied to the experimental electrochemical impedance spectroscopy (EIS) data provides the opportunity for a more detailed study of the resistances of the battery cells. Therefore, the EIS experimental data for both of Li/S cells were analyzed using the tools of EC-Lab V10.32 (Bio-Logic Science Instruments). This analysis could be represented by the best fitting model, consisting of the following multicomponent equivalent circuit:

$$R_o + Q / R_{ct} + W.$$

Here,  $R_o$ ,  $Q$ ,  $R_{ct}$ , and  $W$  are the ohmic resistance at the interface, the constant phase element (CPE), charge transfer

resistance, and the Warburg impedance, respectively. The obtained results are shown in Table 1. As shown in this table, a notable difference in the impedance spectroscopy versus DOD of these cells was observed. Even though both cells show almost the same ohmic and charge transfer resistance values at the beginning of the discharge ( $R_o$  and  $R_{ct}$ ), the ohmic resistance of the cell with the conventional electrolyte reduces as discharge process proceeds, which is directly related to the increase in the concentration of dissolved lithium polysulfides in the electrolyte. Furthermore, the deformation of impedance spectra at points 4–7 of DOD indicates the non-uniform precipitation of low-order polysulfides across the

**Table 1** Values predicted by the equivalent circuit for both Li/S cells during the first discharge process

Point on the DOD graph		1	2	3	4	5	6	7	8
Li/S cell with DOL.DME	$R_o$ (ohm)	14	6	7	3	3	3	3	3
	$R_{ct}$ (ohm)	44	35	29	39	44	44	44	44
Li/S cell with DOL.TTE	$R_o$ (ohm)	11	11	13	13	13	12	12	12
	$R_{ct}$ (ohm)	38	30	45	42	40	33	32	31

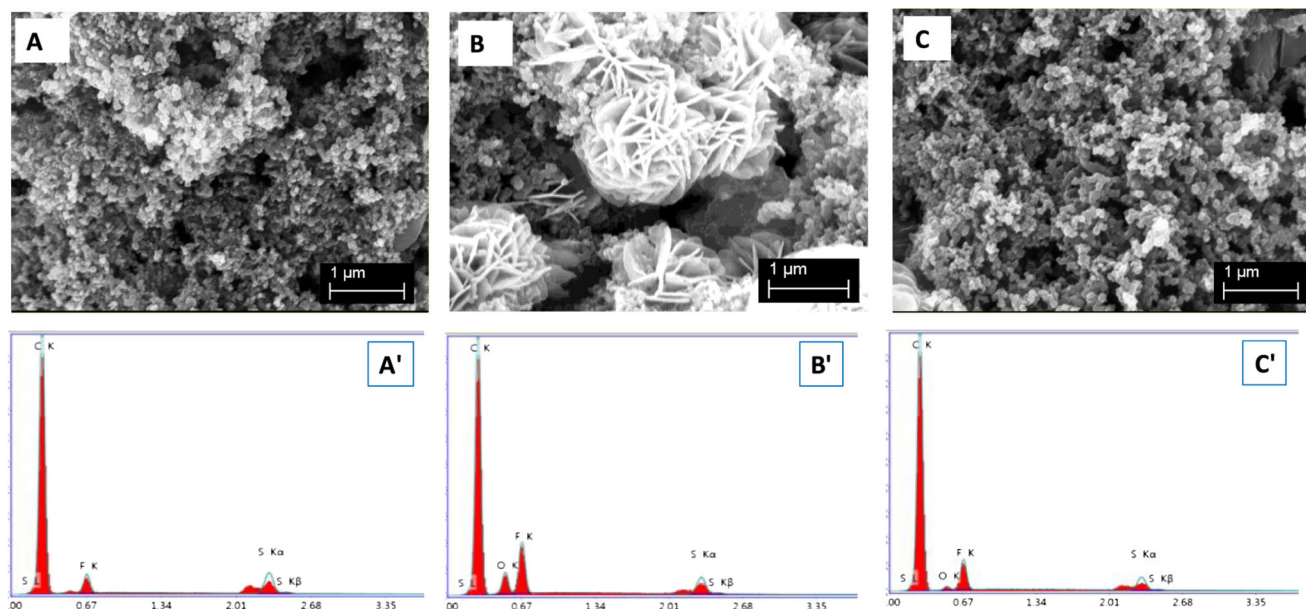


**Fig. 8** SEM images and EDX spectra of pristine S–AHC electrode (**a**, **A'**), discharged S–AHC electrode (**b**, **B'**), and charged S–AHC electrode (**c**, **C'**)

cathode [28, 29], which might be one of the reasons of the fast fading in cyclability of this cell.

The voltage profile for the cell with the fluorinated electrolyte does not completely follow the typical two-plateau profile commonly observed for sulfur–carbon composite cathodes. The first plateau is shorter than the first plateau of the reference cell, and so is the second plateau. However, the ratio of second plateau to first one is almost identical for both cells. For this cell, the first voltage plateau is ascribed to the reduction of elemental and high-order polysulfides. But due to the low concentration of elemental sulfur and high-order polysulfides, the potential drops to second plateau, which is related to the reduction of low-order polysulfides. The third observed plateau might be related to a solid phase reduction reaction [6], or a liquid phase one at low voltages due to the very slow dissolution of active material and very low concentration of dissolved polysulfides.

Interestingly, the cell with the fluorinated electrolyte shows a relatively small increase in its ohmic resistance during the discharge process, which indicates that dissolution of lithium polysulfides into this liquid electrolyte is prevented, this phenomenon is also shown by the larger shift in the second reduction peak in CV curve of this cell. The voltage profile also points out that the fast kinetic of high-order polysulfides reduces the charge transfer resistance at point 2 of DOD, while the coexistence of two phase of active material (high-order polysulfides and low-order ones) and discontinuous phase of high volume fraction of elemental sulfur produces a second circle in impedance spectra. One important note is that although cell voltage plateau and impedance spectra of these two cells are quite different, the delivered capacity is almost identical.

Changes in the morphology of S–AHC cathode electrode in the Li/S cell with the fluorinated electrolyte after first cycle were studied through scanning electron microscopy. Figure 8a shows the SEM image of the pristine S–AHC electrode. At the end of the first discharge process, large flakes of crystal-like discharge products ( $\text{Li}_2\text{S}_2$  and/or  $\text{Li}_2\text{S}$ ) are deposited on the surface of the cathode electrode (Fig. 8b). However, after the first charge process, all of the deposited discharge products disappear and the charged electrode shows morphology similar to the pristine cathode (Fig. 8c), which indicates the full reversibility of electrochemical reaction occurring in this Li/S cell. This was further proved by analyzing the surface of the electrode by energy-dispersive X-ray spectroscopy (EDX), in which the pristine electrode and fully charge one show similar EDX spectra (Fig. 8 (A', C')).

These results indicate that dissolution of lithium polysulfides into the fluorinated liquid electrolyte is prevented; hence active mass loss and parasitic side reactions are eliminated to improve the cyclability and coulombic efficiency of the Li/S cell.

## Conclusions

A low-cost, high-energy lithium–sulfur battery with improved cycling performance was developed by combining a sulfur–hardwood charcoal nanocomposite cathode and a fluorinated liquid electrolyte. This Li/S cell delivered a high initial discharge capacity of  $1260 \text{ mAh g}^{-1}$  and exhibited discharge capacity of  $800 \text{ mAh g}^{-1}$  after 100 cycles at 0.1 C. We further demonstrated the improved cycling performance of this battery cell by comparing the obtained results with a reference



liquid electrolyte commonly used in Li/S batteries. This new Li/S cell maintained stable discharge capacity of 600 mAh g<sup>-1</sup> and coulombic efficiency of 97 % after 300 cycles at 0.3 C, while the reference cell delivered discharged capacity of 230 mAh g<sup>-1</sup> with an efficiency of 80 %. Considering the improved cycling performance of the Li/S cell demonstrated in this work, this battery system seems to be a promising candidate for high-energy and low-cost energy storage systems.

**Acknowledgments** This research was financially supported by Positec, the Natural Sciences and Engineering Research Council of Canada (NSERC), Canadian Foundation for Innovation (CFI), and the Canada Research Chairs (CRC) program.

## References

1. She ZW, Li W, Cha JJ, Zhang G, Yang Y, McDowell MT, Hsu PC, Cui Y (2013) *Nat Commun* 4:1–6
2. Cai K, Song MK, Cairns EJ, Zhang Y (2012) *Nano Lett* 12:6474–6479
3. Li GC, Li GR, Ye SH, Gao XP (2012) *Adv Energy Mater* 2:1238–1245
4. Jeddi K, Ghaznavi M, Chen P (2013) *J Mater Chem* 1:2769–2772
5. Jeddi K, Zhao Y, Zhang Y, Konarov A, Chen P (2013) *J Electrochem Soc* 160:A1052–A1060
6. Ji X, Nazar LF (2010) *J Mater Chem* 20:9821–9826
7. Lin F, Wang J, Jia H, Monroe CW, Yang J, Nuli Y (2013) *J Power Sources* 223:18–22
8. Ji X, Evers S, Black R, Nazar LF (2011) *Nat Commun* 2:325–332
9. Yin L, Wang J, Yang J, Nuli Y (2011) *J Mater Chem* 21:6807–6810
10. Ji X, Lee KT, Nazar LF (2009) *Nat Mater* 8:500–506
11. Yuan L, Yuan H, Qiu X, Chen L, Zhu W (2009) *J Power Sources* 189:1141–1146
12. Wang JZ, Lu L, Choucair M, Stride JA, Xu X, Liu HK (2011) *J Power Sources* 196:7030–7034
13. He G, Ji X, Nazar LF (2011) *Energy Environ Sci* 4:2878–2883
14. Zhang B, Qin X, Li GR, Gao XP (2010) *Energy Environ Sci* 3:1531–1537
15. Fanous J, Wegner M, Grimminger J, Andresen A, Buchmeiser MR (2011) *Chem Mater* 23:5024–5028
16. Wang JL, Yang J, Wan CR, Du K, Xie JY, Xu NX (2013) *Adv Funct Mater* 13:487–492
17. Chao ZS, Lan Z, Yu JH (2011) *J Power Sources* 196:10263–10266
18. Fu YZ, Manthiram A (2012) *RSC Adv* 2:5927–5929
19. Zhang SS (2013) *J Power Sources* 231:153–162
20. Rao MM, Song XY, Cairns EJ (2012) *J Power Sources* 205:474–478
21. Guo JC, Xu YH, Wang CS (2011) *Nano Lett* 11:4288–4294
22. Wu F, Wu SX, Chen RJ, Chen S, Wang GQ (2009) *Chin Chem Lett* 20:1255–1258
23. Ryu HS, Park JW, Park J, Ahn JP, Kim KW, Ahn JH, Nam TH, Wang G, Ahn HJ (2013) *J Mater Chem A* 1:1573–1578
24. Azimi N, Weng W, Takoudis C, Zhang Z (2013) *Electrochem Commun* 37:96–99
25. Gordin ML, Dai F, Chen S, Xu T, Song J, Tang D, Azimi N, Zhang Z, Wang D (2014) *ACS Appl Mater Interfaces* 6:8006–8010
26. Jeddi K, Sarikhani K, Qazvini NT, Chen P (2014) *J Power Sources* 245:656–662
27. Yang Z, Guo J, Das SK, Yu Y, Zhou Z, Abruna HD, Archer LA (2013) *J Mater Chem* 1:1433–1440
28. Ghaznavi M, Chen P (2014) *J Power Sources* 257:394–401
29. Barsoukov E, Macdonald JR, “Impedance Spectroscopy; Theory, Experiment, and Application” second edition, ISBN:0-471-64749-7